Available online at www.sciencedirect.com

ScienceDirect

Advances in Space Research 63 (2019) 1979–1991

ADVANCES IN SPACE RESEARCH (a COSPAR publication)

www.elsevier.com/locate/asr

On the practical exploitation of perturbative effects in low Earth orbit for space debris mitigation

Volker Schaus [a,*], Elisa Maria Alessi [b], Giulia Schettino [b], Alessandro Rossi [b], Enrico Stoll [a]

[a] Institute of Space Systems, Technische Universität Carolo-Wilhelmina zu Braunschweig, Hermann-Blenk-Str. 23, 38108 Braunschweig, Germany
[b] IFAC-CNR, Via Madonna del Piano 10, 50019 Sesto Fiorentino (FI), Italy

Received 9 August 2018; received in revised form 3 January 2019; accepted 14 January 2019
Available online 25 January 2019

Abstract

This paper presents the results of a numerical evaluation of the natural lifetime reduction in low Earth orbit, due to dynamical perturbations. The study considers two values for the area-to-mass ratio, a nominal ratio which resembles a typical value of spacecraft in orbit today, and an enhanced ratio which covers the surface augmentation. The results were obtained with two orbit propagators, one of a semi-analytical nature and the second one using non-averaged equations of motion. The simulations for both propagators were set up similarly to allow comparison. They both use the solar radiation pressure and the secular terms of the geopotential (J_2, J_4 and J_6). The atmospheric drag was turned on and off in both propagators to alternatively study the eccentricity build up and the residual lifetime. The non-averaging case also covers a validation with the full 6×6 geopotential. The results confirm the findings in previous publications, that is, the possibility for de-orbiting from altitudes above the residual atmosphere if a solar sail is deployed at the end-of-life, due to the combined effect of solar radiation pressure and the oblateness of the Earth. At near polar inclinations, shadowing effects can be exploited to the same end. The results obtained with the full, non-averaging propagator revealed additional de-orbiting corridors associated with solar radiation pressure which were not found by previous work on space debris mitigation. The results of both tools are compared for specific initial conditions. For nominal values of area-to-mass ratio, instead, it is confirmed that this resonance effect is negligible.

The paper then puts the findings in the perspective of the current satellite catalogue. It identifies space missions which are currently close to a resonance corridor and shows the orbit evolution within the resonances with a significantly shorter residual orbital lifetime. The paper finishes with a discussion on the exploitation of these effects with regards to the long-term simulation of the space debris environment and a flux and collision probability comparison.

Keywords: Solar radiation pressure; High area-to-mass ratio; Low Earth orbit; Space debris

1. Introduction

Within the research initiative 'Revolutionary design of spacecraft through holistic integration of future technologies' – ReDSHIFT[1] (Rossi et al., 2018), project partners conducted a thorough dynamical mapping of the Earth's orbits from low Earth orbit (LEO) to geostationary Earth orbit (GEO) (see Alessi et al., 2018b; Skoulidou et al., 2017; Colombo and Gkolias, 2017). The common goal of this investigation is to examine natural perturbations which can be beneficial for the disposal of space objects in the context of technical feasibility. One of the investigated effects is the solar radiation pressure (SRP) in LEO.

The main motivation for this work is to prove that the FLORA fast orbit propagator developed by the Institute of Space Systems used for long-term evolution of the space

* Corresponding author.
E-mail addresses: v.schaus@tu-braunschweig.de (V. Schaus), em.alessi@ifac.cnr.it (E.M. Alessi), g.schettino@ifac.cnr.it (G. Schettino), a.rossi@ifac.cnr.it (A. Rossi), e.stoll@tu-braunschweig.de (E. Stoll).

[1] http://redshift-h2020.eu.

https://doi.org/10.1016/j.asr.2019.01.020
0273-1177/

debris environment can safely recognize these resonances. Once proven, long-term simulations of the space debris environment can be used to investigate scenarios in which the SRP resonance corridors are targeted at the end-of-life and thus exploit the effect for mission disposal. The relevant perturbations for these beneficial conditions are the oblateness of the Earth (J_2 term) in combination with a model for the SRP. Both effects are considered in the semi-analytical orbit propagator. Thus, it can be reproduced.

The underlying theory and existence of the SRP induced perturbations is well-known and has been studied to a great extent. It dates back to the 1960s where observed perigee variations of Echo 1 and Vanguard 1 could be explained with the effect of solar radiation pressure (viz., Parkinson et al., 1960; Musen, 1960). Cook gave a first graphical representation of the location of SRP resonances for semi-major axis and inclination (Cook, 1962, rf. Fig. 5). For further insight, the reader is pointed to Alessi et al. (2018b), which contains a thorough review of the SRP perturbation theory. A broader assessment of natural end-of-life solutions including solar and lunisolar gravitational perturbations, higher-degree zonal harmonics of Earth's gravitational potential, and SRP is given in Alessi et al. (2018a). Broadening to other orbit regimes, special end-of-life disposal strategies for dedicated missions in libration point orbits (LPO) and high eccentricity orbits (HEO) were examined in Colombo et al. (2015). Medium Earth orbit (MEO), where navigational constellations reside, were studied in Alessi et al. (2014) and Lücking et al. (2012).

The theory describes six resonance cases affecting the eccentricity which are defined by the following equation taken from Alessi et al. (2018b).

$$\dot{\Psi}_j = n_1\dot{\Omega} + n_2\dot{\omega} + n_3\dot{\lambda}_s \stackrel{!}{=} 0 \quad (1)$$

In Eq. (1), $\dot{\Omega}$ is the rate of precession of the right ascension of the ascending note, $\dot{\omega}$ is the rate of precession of the argument of the perigee and $\dot{\lambda}_s$ is the rate of change of the angle towards the Sun. The coefficients n_i are used to distinguish the six cases, $n_1 \in \{0, 1\}, n_2 \in \{-1, +1\}$ and $n_3 \in \{-1, +1\}$. This leads to the following six conditions where the resonances occur, listed in descending order of magnitude in the eccentricity effect:

$$\begin{aligned}
\dot{\Psi}_1 &= \dot{\Omega} + \dot{\omega} - \dot{\lambda}_s \stackrel{!}{=} 0 \\
\dot{\Psi}_2 &= \dot{\Omega} - \dot{\omega} - \dot{\lambda}_s \stackrel{!}{=} 0 \\
\dot{\Psi}_3 &= \dot{\omega} - \dot{\lambda}_s \stackrel{!}{=} 0 \\
\dot{\Psi}_4 &= \dot{\omega} + \dot{\lambda}_s \stackrel{!}{=} 0 \\
\dot{\Psi}_5 &= \dot{\Omega} + \dot{\omega} + \dot{\lambda}_s \stackrel{!}{=} 0 \\
\dot{\Psi}_6 &= \dot{\Omega} - \dot{\omega} + \dot{\lambda}_s \stackrel{!}{=} 0
\end{aligned} \quad (2)$$

1.1. Fast long-term orbit analysis (FLORA)

The standard propagator used for the long-term simulations is called FLORA. FLORA stands for fast, long-term orbit analysis and is an in-house development of the Institute of Space Systems. It uses only analytical equations and omits short-periodic variations. Therefore, it is especially well-suited for fast, long-term orbit predictions. The single perturbations are implemented in separate subroutines and can be turned on and off by the user as desired. More details on the equations, models and implementation can be found in Möckel (2015) and Flegel (2007). The perturbations present in FLORA are:

- **Atmospheric Model:** The effect of Earth's atmosphere in FLORA is based on the NRLMSISE-00 model, analytical perturbation equations by King-Hele and the space weather data provided by Celestrak/Dr. T.S. Kelso. The implementation is optimized for runtime and uses several pre-computed look-up tables. For instance, one table is present retrieving the atmospheric density and scale height of the NRLMSISE-00 model. The atmospheric density is respected in the software up to an altitude of 4000 km.
- **Third Body Perturbations:** Third body gravitational effects of the Sun and the Moon are considered. The implemented follow the analytical equations for third-body perturbations as per Vallado (2013), p. 681, Eq. 9–54.
- **Solar Radiation Pressure:** The solar radiation pressure is assumed to be constant. The acceleration forces are only dependent on the characteristics of the satellite, namely the reflectivity and the area-to-mass ratio. Earth's shadow is considered by evaluating Escobal's shadow function (Escobal, 1965).
- **Gravitational Potential of the Earth:** The implementation only uses zonal harmonics terms J_2, J_4 and J_6. Sectorial and tesseral harmonics are omitted.

1.2. NEPTUNE

Opposed to the fast (semi-)analytical propagator, NEPTUNE is a high-fidelity propagator, which uses numerical integration for the equations of motion. It was developed for accurate orbit propagation required by future space surveillance systems. The major part of the implementation was supported by ESA's Networking/Partnering Initiative (NPI). Currently, the Institute of Space Systems maintains and further develops the propagator. According to Braun (2017), the most complete source of information on NEPTUNE, the propagator considers the following force models:

- **Atmospheric Model:** Neptune uses also the NRLMSISE-00 model.

- **Third Body Perturbations:** Third body gravitational effects of the Sun and the Moon are considered. The implementation normally uses the DE405 and DE421 ephemerides for solar system bodies. However, these ephemeris files only contain entries up to the years 2050 and 2053, respectively. This was insufficient for the 120 years simulation time frame of this SRP evaluation study. Therefore, NEPTUNE was updated to use the ephemeris DE430. As for the previously used ephemeris files, a subset of DE430 with reduced annual coverage was used (1850–2150).
- **Solar Radiation Pressure:** The solar radiation pressure incorporates seasonal variations due to the change in distance between Sun and Earth. Satellites entering and existing Earth penumbral and umbral eclipse regions are calculated using a conical volume based upon a spherical Earth model.
- **Gravitational Potential of the Earth:** In NEPTUNE the user can select one of three gravitational models, EIGEN-GL04C, EGM96 and EGM2008. For the simulations in this paper only EIGEN-GL04C was chosen. The degree of the model can also be selected by the user. When comparing residual life time, the degree and order were set to 6×6. For all other gravity modeling in this paper, simulations were configured to only use zonal harmonics terms J_2, J_4 and J_6 in order to allow comparison with the results from the analytical propagation with FLORA.

NEPTUNE does cover additional perturbations, such as models for Earth's albedo, Solid Earth tides, polar tides and ocean tides. These were neglected in this study, to facilitate model comparisons and reduce computational burden.

2. Numerical evaluation of the SRP resonances

In order to reproduce the SRP resonance maps presented in Alessi et al. (2018b), several simulations were conducted. To allow direct comparison between the results, almost all the input parameters were set to the exact same values as in Alessi et al. (2018b).

The simulations were all set up in a similar fashion. The start date of the simulations was set to 21st of June 2020 6:43:13, the beginning of the astronomical summer where the longitude of the Sun in the ecliptic plane is $\lambda_S = 90.086°$. Each set of initial orbital elements was propagated over 120 years.

The input conditions were varied to sweep the complete LEO region. They covered the following values:

- semi-major axis $a \in \{6700, 6710, \ldots, 9500\}$ km (10 km steps)
- eccentricity fixed to $e = 0.01$
- inclination $i \in \{0, 0.2, \ldots, 120\}^\circ$ (0.2° steps)
- RAAN fixed to $\Omega = 0°$
- argument of the perigee fixed to $\omega = 0°$
- Two cases for the area-to-mass ratio:A nominal value of $A/m = 0.012\ \mathrm{m^2\ kg^{-1}}$, which represents a common ratio of satellites without any area increasing device and an enhanced value of $A/m = 1.0\ \mathrm{m^2\ kg^{-1}}$, which is considered to reflect sail sizes of current projects for small satellites (Colombo et al., 2017).

Initial conditions were varied and perturbations individually enabled and disabled to highlight distinct effects. FLORA was first configured to only use the zonal harmonics J_2, J_4 and J_6 of the Geopotential and the SRP model. This was done to clearly show the SRP resonance corridors in all altitude regimes, cf. Fig. 1 top plot. All possible perturbations in FLORA were then activated (see Section 1.1 in the introduction) to be able to examine the possibility of cancellation effects. Typically, as satellites are entering in lower altitudes, atmospheric drag leads to a circularization of the orbit (reducing the eccentricity towards zero). This counteracts the desired effect of the eccentricity increase to facilitate SRP resonances. This case is used to ensure that the J_2/SRP resonance is actually leading to shorter residual orbital lifetimes in combination with the atmospheric drag. The result of these simulations forms the basis for the residual lifetime plots, cf. Fig. 1 bottom plot.

2.1. Nominal area-to-mass ratio

Fig. 1 shows the results of the FLORA simulations with nominal A/m ratio. The semi-major axis is plotted over the inclination in both plots. The color bar of the top plot indicates the maximum eccentricity values, which were recorded during 120 years of simulation. In the nominal case only the two strongest resonances (Ψ_1 and Ψ_2) develop as faint lines. The color bar of the bottom plot of Fig. 1 depicts the residual in-orbit lifetime. It shows that atmospheric drag reduces residual lifetime up to $a = 7100$ km over the whole inclination range (yellow to purple region). Objects with a larger semi-major axis are not re-entering which corresponds to the large black region in the plot. The slight eccentricity built-up cannot be exploited in this case and does not lead to regions with shorter lifetimes along the resonances. It should be noted that there is also a slight increase in the orbital lifetime over inclination due to atmospheric drag only, as described in Oltrogge and Chao (2007), p. 11. This was not examined further in this work, because the focus was explicitly on studying re-entry possibilities apart from drag.

2.2. Enhanced area-to-mass ratio

This is different for the second case of simulations with the increased A/m ratio as shown in Fig. 2. The top plot depicts the maximum eccentricity values. The color bar now ranges from $e = 0.01$, which corresponds to the initial condition, up to $e = 0.3$. Several resonance regions emerge. Most of them can be mapped to the analytical predictions

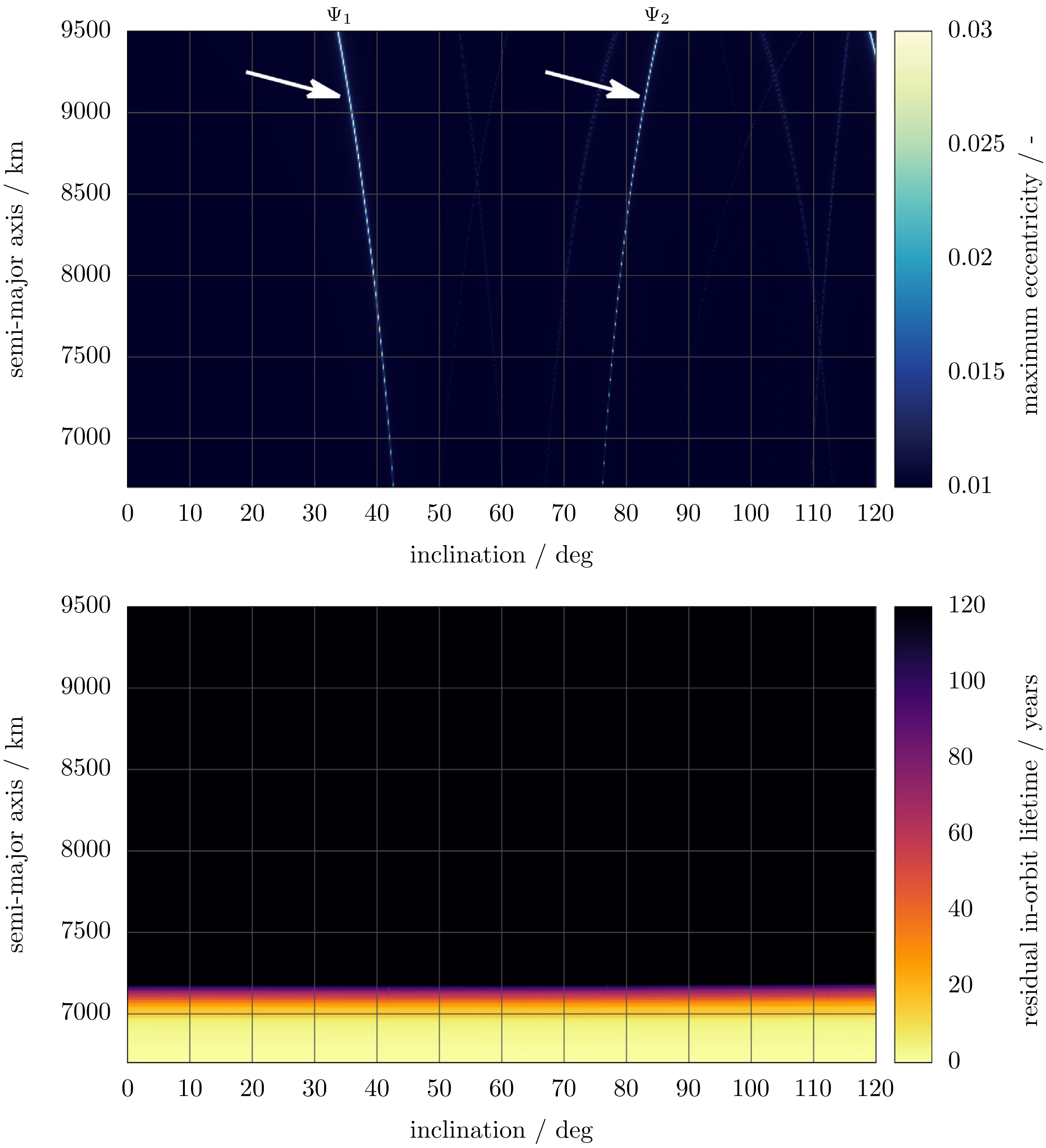

Fig. 1. SRP resonance modeled with FLORA with nominal A/m ratio: The top plot shows the maximum eccentricity built-up over 120 years. Only the two strongest resonances develop as faint lines in the top plot with an eccentricity built-up from $e = 0.01 - 0.03$. The plot at the bottom depicts the residual in-orbit lifetime. It clearly shows that only the atmospheric drag leads to shorter orbital lifetimes up to $a = 7100$ km and no object above is re-entering within 120 years.

described in Alessi et al. (2018b), cf. Eq. (2). The resonances Ψ_1 to Ψ_5 are all present at the expected positions in the a-i space. The two resonances intersecting the abscissa at 110° and 112° are symmetric continuations of Ψ_4 and Ψ_1. It is worth noting that the postulated resonance Ψ_6 in the range from 62° and 72° inclination is not a distinct feature for the chosen color range of the eccentricity build-up. Since Ψ_6 is the weakest of the resonances, it was necessary to adjust the sensitivity of the eccentricity color scale to $e = 0.08$ in order to increase legibility. It turns out that the resonance is present then and the respective plot can be found in the annex (Fig. A.9).

Interestingly, as one resonance seems missing, new ones appear. In the inclination range from 80° to 110°, where many of the polar space missions operate, additional faint eccentricity built-up lines emerge. One line in parallel to Ψ_2 from 80° to 88°; and two more overlapping at 90° and a semi-major axis of $a = 7500$ km. Their origin is due to the effects of the shadow of the Earth and was not found elsewhere in previous work. Results from comparison simulations in which the shadow was turned off can be found in the annex (Fig. A.10). An analytical description of the shadow effect in combination with the SRP remains to be done and is beyond the scope of this paper. The order of

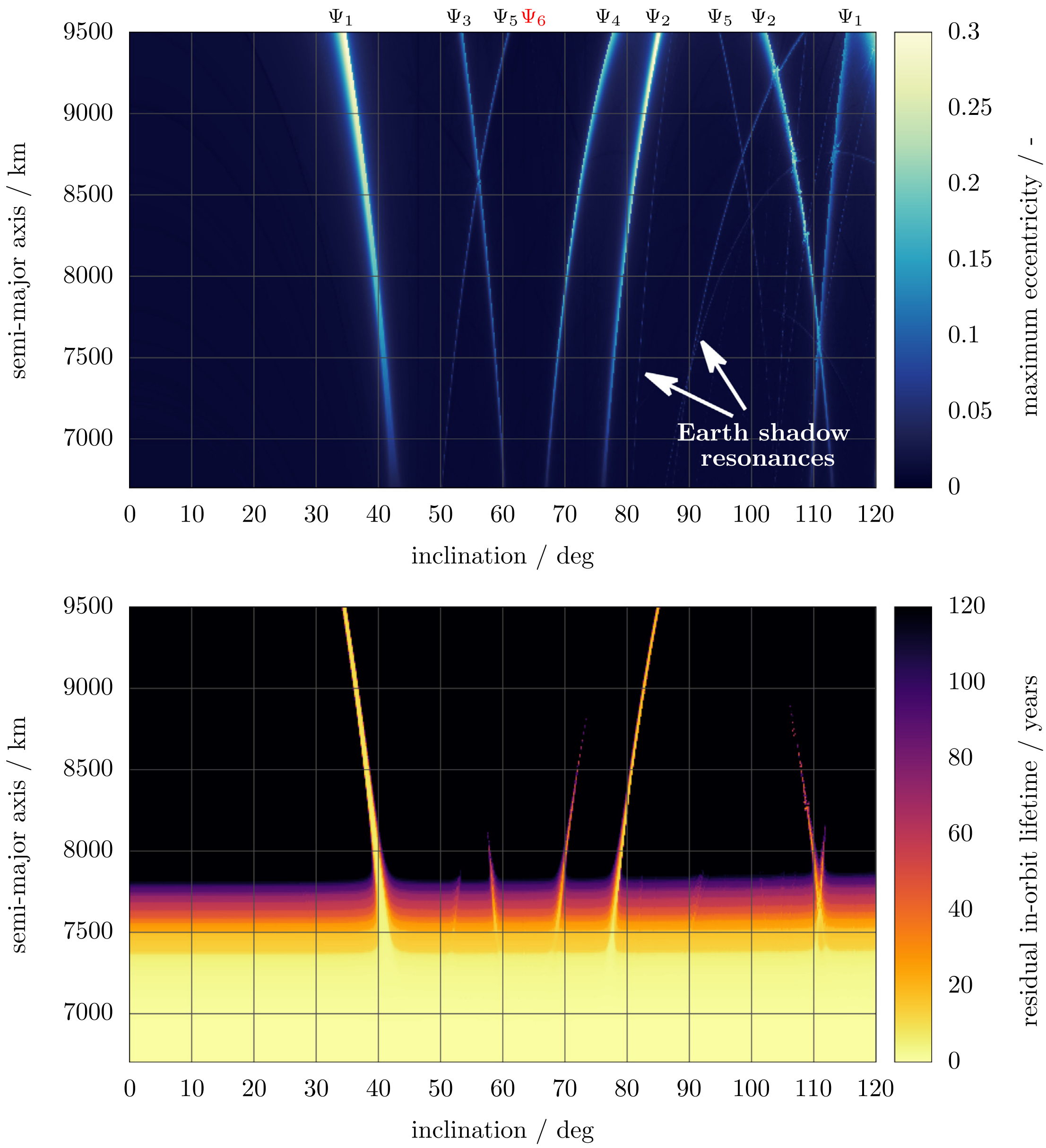

Fig. 2. SRP resonance modeled by FLORA for a larger A/m ratio: The top plot shows the maximum eccentricity built-up over 120 years, the color code is set to the range from $e = 0.01 - 0.3$. All resonances develop except, although the sixth one is too weak to appear. Additional resonances appear due to Earth shadowing effects. The eccentricity increase leads to shorter lifetimes along the resonances, as can be seen in the bottom plot. Corridors of reduced in-orbit lifetime emerge along the resonances, and of course the boundary for exploiting just the atmospheric drag is raised and widened.

magnitude of the Earth shadow resonances is low and therefore they are of minor practical importance. This can be seen by looking at the bottom plot of Fig. 2 showing the residual in-orbit lifetimes. In comparison to Fig. 1, now that the area-to-mass ratio is increased, missions up to $a = 7700$ km benefit from the atmospheric drag. In addition, distinct re-entry corridors appear with significantly shorter life times. Comparing the top plot to the bottom plot, they clearly correspond to the J_2 and SRP resonances. The plot shows that re-entering is generally possible along certain corridors. For the two strongest resonances, a re-entry can be achieved up to semi-major axis $a = 9500$ km in reasonable time frames of 20–30 years. The weaker resonances fade out sooner. In contrast, the overlapping Earth shadow resonances at 90° inclination are only visible as a slight disturbance in the widened transitional band of the atmospheric drag ($a \in [7500, 7800]$ km).

2.3. Comparison between the semi-analytical FLORA and the high-fidelity NEPTUNE propagator

The results retrieved from FLORA, the fast semi-analytical propagator mainly used propagating large sets of space objects over long periods were cross-validated against the high-fidelity propagator NEPTUNE. The results of this comparison are depicted in Fig. 3. As in

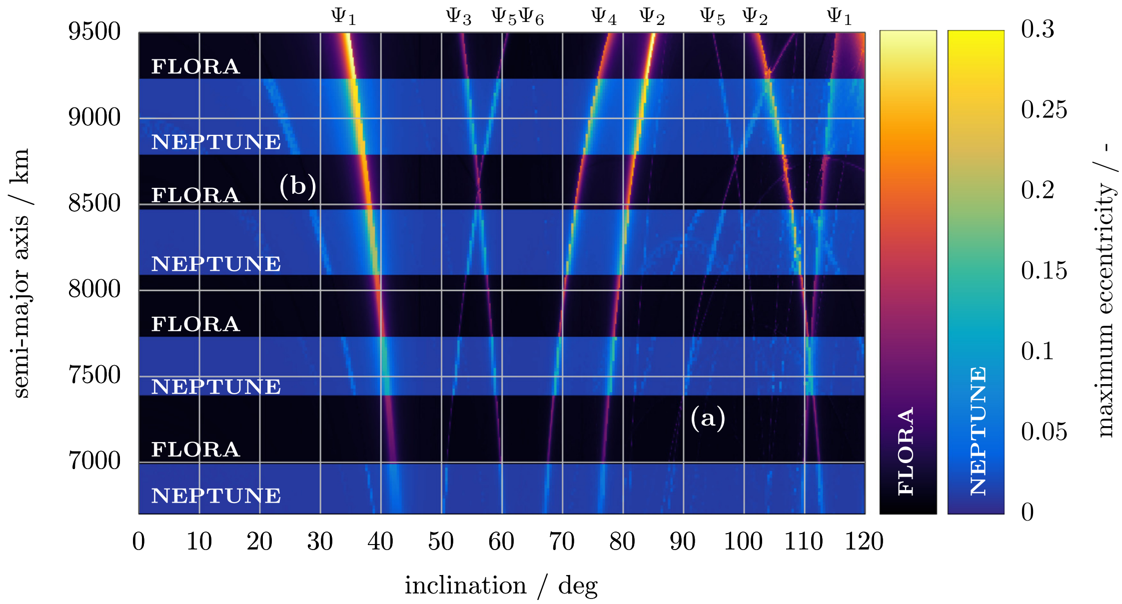

Fig. 3. The plot shows a comparison of FLORA and NEPTUNE results. The data is color-coded differently according to its origin: FLORA uses a transition from black over red to yellow and NEPTUNE uses dark-blue over green to yellow. The plot presents the result in stripes so that the existence and the location of the resonances can be validated. (For interpretation of the references to color in this figure legend, the reader is referred to the web version of this article.)

the previous plots, the color-coded graph indicates the maximum eccentricity recorded during 120 years of simulation time as a function of semi-major axis and eccentricity. The plot distinguishes the results from FLORA and NEPTUNE with different color palettes. The results from both propagators are organized in stripes along the semi-major axis over the full inclination range. FLORA uses a color palette ranging from black to red to yellow; whereas NEPTUNE uses a color palette starting with dark blue over green to yellow. This presentation allows for easy comparison between the results of both tools. One can visually track the continuation of the resonances across the stripes and assess if the resonances are at the expected location, if they appear at all, and if they have a similar order of magnitude. Due to computational restrictions, the high-fidelity simulations used a coarser grid of initial conditions. In essence, the resolution was reduced by a factor of four meaning an inclination step size of 0.4° and a semi-major axis step size of 20 km. To a large extent the NEPTUNE results match very well to the FLORA results. All the six resonances (even the weak Ψ_6) are present and the patterns for the Earth shadow resonances continue over the stripes of the plot, see labels above the plot and in the high inclination region label (a). With NEPTUNE, another resonance appears left of Ψ_1 between 20° and 38° inclination, see label (b). This one is not present in the FLORA results. Shadowing effects can be ruled out as this resonance persisted during an evaluation in which the shadowing equations have been neglected in NEPTUNE. Its origin has to be studied further.

3. Exploiting the resonances

3.1. Strategy for impulsive maneuver

The low area-to-mass ratios typical of today's spacecraft preclude the use of SRP resonances as an effective orbit lifetime reduction.

In case of cross-section augmentation by a solar sail, the majority of the current missions in LEO would benefit from a sail. Fig. 4 shows the residual lifetime as in Fig. 2 with an overlay of the location of the payloads as contained in the MASTER model for the 2013 reference epoch. For Fig. 4, the content of the MASTER model was filtered to contain only payloads. Additionally, all entries with a semi-major axis $a > 9500$ km were neglected. The resulting sub-population contains a total of 2064 payloads. These objects were propagated with FLORA for 25 years in order to assess the natural compliance to the IADC 25-year rule (IADC, 2007). The propagator marked 1347 as re-entered at the end of the simulation. This corresponds to 65.262% of the population.

However, looking at Fig. 4 the acting principle for the re-entering of almost 2/3 of the payloads is the aerodynamic drag. Therefore, any sail attached to a payload in that altitude has to be operated as a drag sail. The orientation of the sail has to be perpendicular to the flight path to maximize the reduction in lifetime, which was assumed for this study.

For higher altitudes, the SRP resonance can be exploited by high area-to-mass ratios. The paper shows

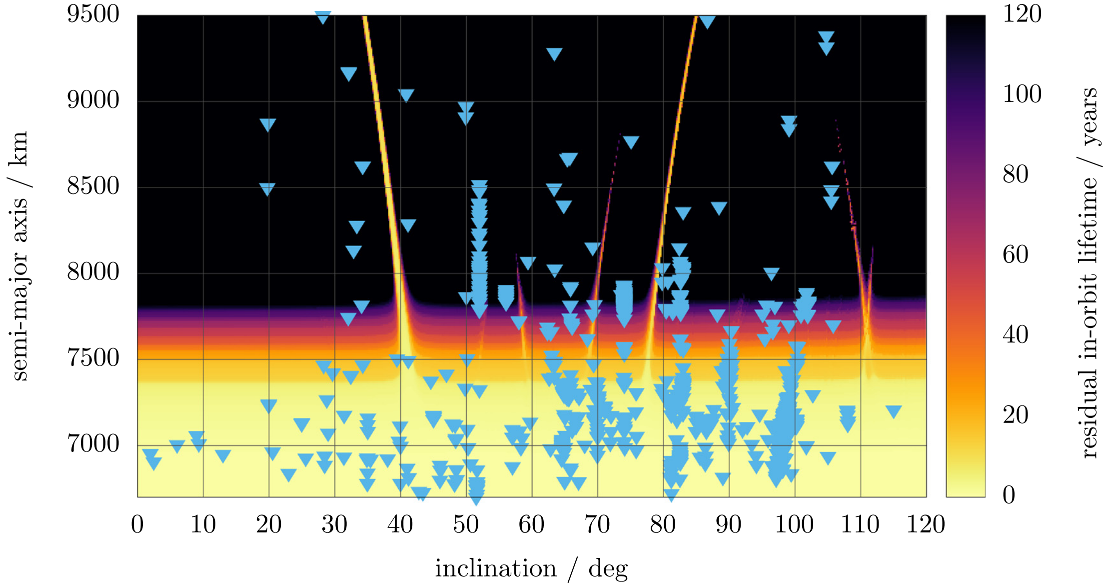

Fig. 4. In-orbit lifetime map for the enhanced A/m ratio. The blue triangles correspond to the payloads in space according to the MASTER model for the reference epoch 2013. (For interpretation of the references to color in this figure legend, the reader is referred to the web version of this article.)

the results for 1.0 $m^2\,kg^{-1}$. These high values for area-to-mass are only achievable on micro satellites (kilogram boundary, and example mission). At the moment the technology for solar sails has not reached the level of deploying sails with large areas (100–200 m^2). This requirement on the sail size assumes that the sail is actively controlled and pointed perpendicular to the Sun when the eccentricity built-up is beneficial for shorter orbital lifetime. Active sail control puts a lot of additional effort on the mission operations (just for de-orbiting). If instead a passive sail were used and the satellite were a free tumbling mode, the required area of the sail would need to be increased by a factor of 2, in accordance to Cauchy's formula on the projected area of thin plates (see e.g. Moxnes et al., 2017, Eq. (6)).

From Fig. 4, it is possible to select certain space objects which reside in or close enough to a resonance corridor already. The selection process used to identify possible target missions is a combination of considering orbit mechanics for maneuvers and visual inspection. As a first approximation of the order of magnitude of the required Δv, the Gauss planetary equations can be used (see e.g. Vallado, 2013, Eq. (9–18), (9–20) and (9–21)).

$$\begin{aligned}\Delta a &= 2\frac{e\ sinf}{n\sqrt{1-e^2}}\Delta v_r + 2\frac{(1+e\ cosf)}{n\sqrt{1-e^2}}\Delta v_t\\ \Delta e &= \frac{\sqrt{1-e^2}}{n\ a}[sinf\ \Delta v_r + (cosf + cosE)\Delta v_t]\\ \Delta i &= \frac{r}{h}\ cosu\ \Delta v_h\end{aligned} \tag{3}$$

where a is the semi-major axis, e is the eccentricity, i is the inclination, f is the true anomaly, n is the mean motion, u is the argument of the latitude, r is the radius, E is the eccentric anomaly, and h is the angular momentum. In essence, these equations put the change in the orbital elements (semi-major axis Δa, eccentricity Δe and inclination Δi) in relation to a disturbing force, specifically accelerations applied in an impulsive, single burn maneuver. This maneuver can be defined as a velocity vector $\Delta v = (\Delta v_r\ \Delta v_t\ \Delta v_h)^T$. The first two elements of this vector correspond to a velocity change inside the orbital plane, in radial (subscript r) and transversal (subscript t) direction. The third component is perpendicular (subscript h) and points in out-of-plane direction. Looking at Eq. (3), it is apparent that the inclination change Δi is decoupled from the in-plane maneuver changing the semi-major axis and the eccentricity. Changes of the inclination in LEO are generally expensive compared to the in-plane maneuvers. In the special case of a circular orbit, a 1° change in inclination requires $\Delta v = 127\ m\,s^{-1}$ for a radius of 9500 km.

The first two equations for the maneuver inside the orbital plane can be rewritten as linear equation system with two unknowns, namely

$$\begin{pmatrix}\Delta a\\ \Delta e\end{pmatrix} = \begin{pmatrix}2\frac{e\ sinf}{n\sqrt{1-e^2}} & 2\frac{(1+e\ cosf)}{n\sqrt{1-e^2}}\\ \frac{\sqrt{1-e^2}\ sinf}{n\ a} & \frac{\sqrt{1-e^2}(cosf+cosE)}{n\ a}\end{pmatrix}\cdot\begin{pmatrix}\Delta v_r\\ \Delta v_t\end{pmatrix}. \tag{4}$$

Solving these equations for a required change of the semi-major axis Δa and change in eccentricity Δe to reach a re-entry corridor from a given initial orbit allows the calculation of the estimate for the Δv.

3.2. Application to real missions

Fig. 5 shows a selection of three objects whose orbital evolution and the maneuver to reach the resonance is examined further. Although the objects correspond to actual payloads in space today, this is of minor importance because they cannot exploit the SRP effect. The analysis

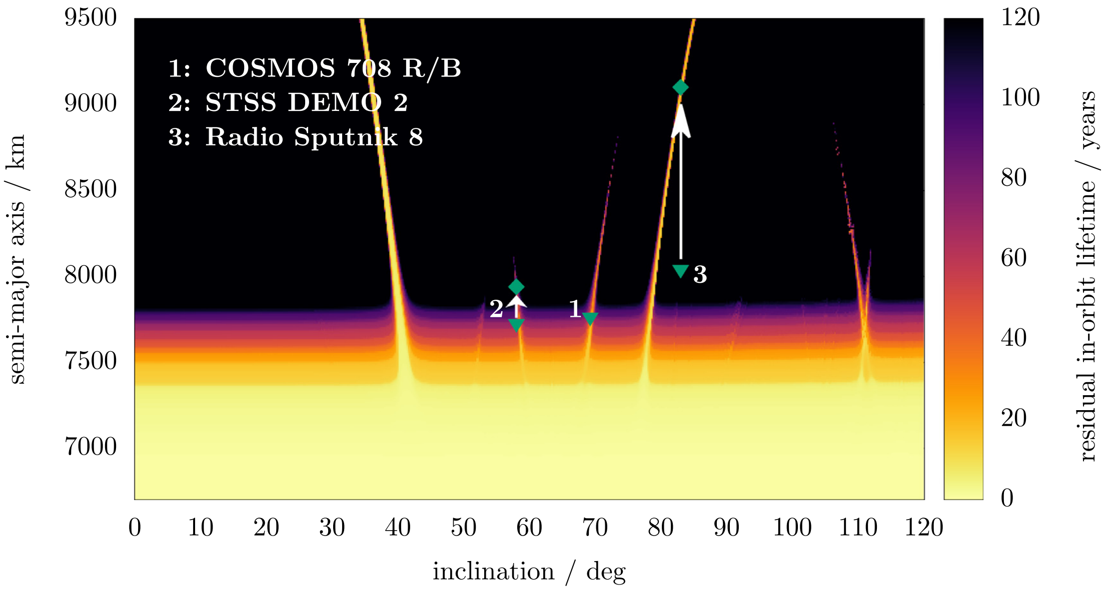

Fig. 5. Selected space objects and their maneuver to target the resonance.

shows that looking at the catalog of space objects today, there are missions in the vicinity of the resonances.

The first object corresponds to a COSMOS upper stage. It is very close to a resonance, and it already has the matching value of the inclination i. The Δv for a maneuver to place it into a resonance region by slightly increasing eccentricity and decreasing semi-major axis by 20 km as given in Table 1.

The second object is the STSS DEMO 2 mission. It can be positioned inside a resonance corridor again by adjusting the eccentricity as in the first case and by raising the semi-major axis by 220 km. This can be achieved by an in-plane maneuver of approximately 52 m s^{-1} (see Table 1).

The third object at 83° inclination corresponds to a small radio satellite (Radio Sputnik 8). Here, the indicated raise of the semi-major axis from 8040 km to 9100 km and the required Δv of 176 m s^{-1} is likely not feasible. Yet, this case demonstrates clearly the potential of re-entering from high LEO within reasonable time frames. Fig. 6 shows the evolution of semi-major axis, eccentricity and inclination over time. The plots show two data sets each, one from the propagation with FLORA (red data series) and the other from NEPTUNE (green data series). The semi-major axis decreases only slowly for about 15 years. In this time the eccentricity climbs to a value of about 0.2. After that, the orbit's pericenter is so low that the atmosphere leads to circularization and ultimately to the de-orbit. Both propagators used a geodetic altitude of 100 km as cut-off criteria for the re-entering of the object to Earth. With FLORA, the object re-enters after 22 years, and NEPTUNE calculates an even shorter in-orbit time of just 18 years. The third plot shows a decrease in inclination, which corresponds well to the shape of the resonance Ψ_2 (c.f. Fig. 2). This highlights the fact that the orbit evolution moves along the resonance. It is worth mentioning that the initial condition for the semi-major axis is slightly different for FLORA and NEPTUNE. FLORA used a value of $a = 9100.4$ km whereas NEPTUNE picked-up the resonance at $a = 9060.4$ km.

For completeness, the orbit evolution for the COSMOS upper stage in the resonance Ψ_4 is given in the Appendix in Fig. A.8.

To exploit these re-entry corridors (demonstrated by long-term simulations of the space debris environment), two different implementations are conceivable. First, the analytical equations of the corridors can be used directly.

Table 1
Overview of the selected payloads initial and target condition for SRP de-orbiting.

	Object 1 COSMOS 708	Object 2 STSS Demo 2	Object 3 R/Sput. 8
NORAD ID	7663	35937	12998
COSPAR ID	1975-012A	2009-052A	1981-120B
$A_{nom.}$/m^2	3.5016	28.5789	0.8705
$A_{enh.}$/m^2	644.20	4580.0	39.64
$a_{initial}$/km	7765.5	7722.5	8042.4
a_{target}/km	7745.5	7940.0	9100.4
Δa /km	20.0	217.5	1058.0
$e_{initial}$/–	0.0026	0.0004	0.0019
e_{target}/–	0.01	0.01	0.01
Δe/–	0.0074	0.0096	0.0081
$i_{initial}$/°	69.23	58.00	82.96
Ω/°	150.4	269.00	261.19
ω/°	354.53	224.24	84.66
M/°	292.35	193.83	321.61
Δv_r/m s^{-1}	−10.32	−51.92	162.0
Δv_t/m s^{-1}	−1.49	0.735	70.3
Δv_{total}/m s^{-1}	10.43	51.92	176.3

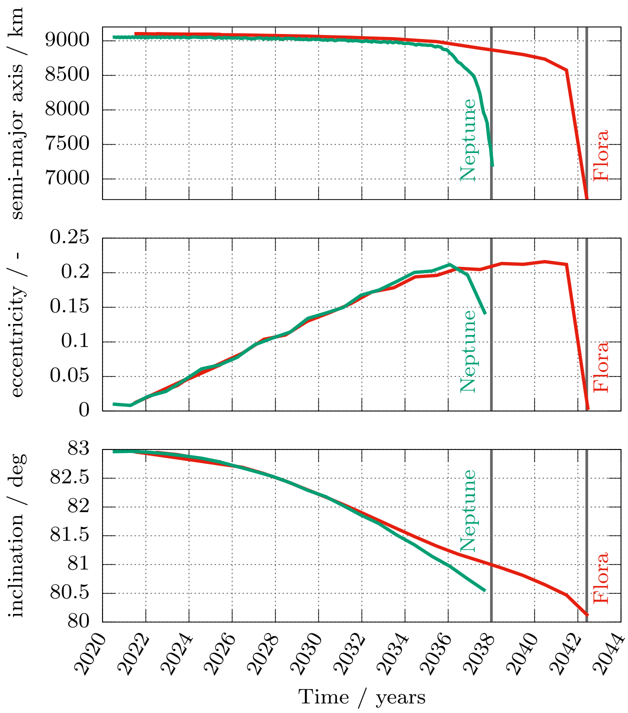

Fig. 6. Orbit evolution inside the resonance Ψ_2, Object 3 of Table 1: The parameters defining the shape of the orbit, semi-major axis, eccentricity, and inclination, are depicted over time. The plots contain results from FLORA in red and NEPTUNE in green. Both propagators show very similar orbit evolution and re-enter within 18 years for NEPTUNE respectively 22 years for FLORA, which is compliant to the 25-year-rule of the IADC space debris mitigation guidelines. (For interpretation of the references to color in this figure legend, the reader is referred to the web version of this article.)

Second, the maps coming from the simulation results can be stored as look-up tables which are then targeted for missions which should de-orbit using the J_2/SRP resonance. This will be decided on during the next phase of the ReDSHIFT project.

4. Flux and collision probability assessment

The last section of the paper focusses on the debris environment that the target object experiences over the disposal decay period and its associated collision probability estimates. Given that certain regions are more densely populated than others, it is important to analyze the flux on objects which exploit a resonance and reenter faster. For example, these objects cross for example the altitude of 800 km to 900 km, they encounter a higher flux. The flux on the faster decaying routes will be compared to the case where the objects remain unchanged in their orbital position as in the catalogue. In essence, this section compares two counteracting strategies: (1) staying in orbit for a long time (likely 120 years or more); and (2) increasing the area-to-mass ratio and crossing densely populated regions and re-entering in 20–40 years. The section again uses orbital information of the three objects introduced in Section 3.2.

The future populations of space objects and debris used for this analysis originate from the baseline reference scenario conducted in the first year of the project ReDSHIFT. The simulation campaign covered various different variations on the input parameters. The baseline reference case is in many ways compliant to the IADC space debris mitigation guidelines (IADC, 2007). This is still considered optimistic when looking at the actual compliance level today. The baseline reference used a repeating launch traffic of the years 2005–2012, a rather low period. The collision avoidance success rate was assumed to be 80% against trackable debris (10 cm in LEO and 1 m in GEO). Regarding post mission disposal, in LEO 60% of the non-compliant objects performed an end-of-life maneuver to an eccentric orbit with 25 years life time. In GEO, the satellites were placed in a graveyard orbit. The scenario also considered 2–3 self-induced in-orbit explosions for the first 15 years starting at the year 2013. More details on the baseline case and the variations performed can be found in Schaus et al. (2017).

The most important data output of these simulations are annual populations. For the flux assessment, annual population files from 50 Monte Carlo runs of the baseline reference scenario were merged and scaled accordingly. This served directly as input to a special tailored version of our Long-Term Utility for Collision Analysis (LUCA), a long-term simulation tool of the space debris environment. This tailored version will be incorporated in the overall software deliverable of the ReDSHIFT project. It is capable of calculating the annual flux on a given target orbit. This is done by calculating the collision rate of the target of interest with the so-called orbit trace method (see, e.g., Öpik, 1951). In addition to that, a second validation was performed with the ESA MASTER software. The standard version of this software suite however contains a different scenario and cannot perform analyses of up to 120 years' duration. In order to overcome these limitations, the combined results of the reference simulation were further processed to assess spatial density as a function of altitude shell. The standard MASTER data base was then replaced by the new reference data coming from the ReDSHIFT simulation.

With two alternatives for the flux calculation at hand (MASTER and the tailored LUCA version), the flux on the three example missions presented in Section 3.2 can be compared. The comparison covers in each case the original orbit with the nominal cross-sectional area and the initial orbit condition to detect resonances with enhanced area-to-mass ratio. The results of the flux comparison are presented in Fig. 7. Each plot corresponds to one object and features four data series giving the annual flux per square meter. The black and green data represents the nominal area-to-mass ratio case from LUCA and MASTER. The red and purple data represents the enhanced area-to-mass ratio case from LUCA and MASTER. For this case the orbit was propagated with the FLORA propagator directly in the LUCA simulation run. Annual snapshots of the orbital ele-

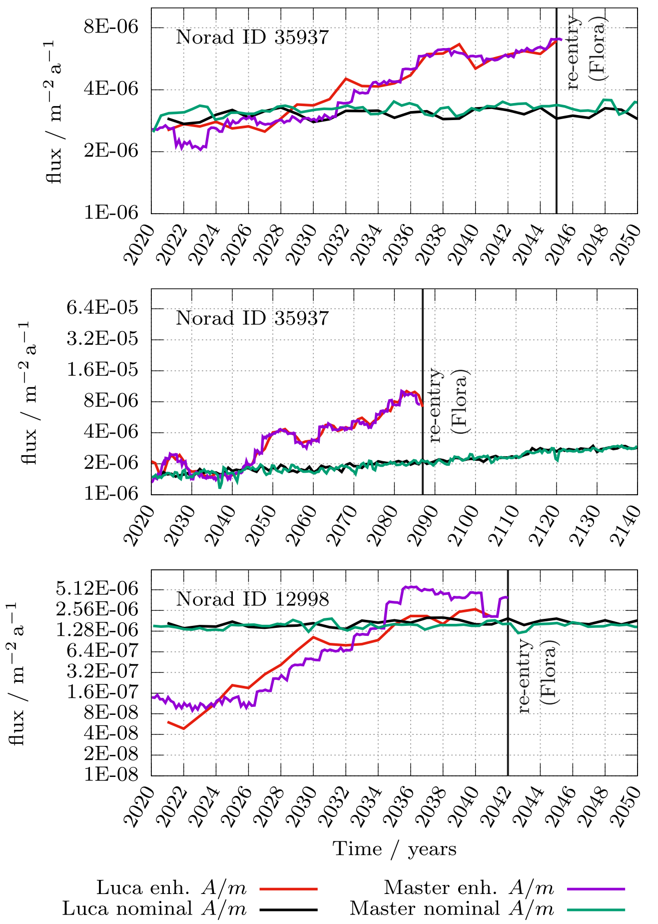

Fig. 7. Annual flux per square meter comparison of the three example objects: black – LUCA results with nominal A/m ratio; green – MASTER results with nominal A/m ratio; red – LUCA results with enhanced A/m ratio; purple – MASTER results with enhanced A/m ratio. LUCA used the orbit-trace algorithm for the collision rate determination. MASTER used the altitude bin approach with spatial density. (For interpretation of the references to color in this figure legend, the reader is referred to the web version of this article.)

ments were used as input for the flux assessment with MASTER. MASTER is capable of using 50 entry sets for orbit evolution over time in its input file. The re-entry epoch is marked in all the plots with a vertical line and label. It corresponds to the epoch in which the FLORA propagator marked the object as re-entered. In all three plots, the flux calculation matches very well for the two cases. This means that the underlying algorithms are tuned very well and reproduce similar results. It is an important validation step for the software deliverable in ReDSHIFT which contains the flux calculation.

The flux values can be used to calculate collision probabilities for the actual space mission with the following equations taken from Klinkrad (2006), page 61, Eq. 3.1–3.3. The collision rate can be expressed by

$$c = F \cdot A \cdot \Delta t \tag{5}$$

where F is the flux, A is the cross-section and Δt is the time interval spent in the region with the flux F. Typically LUCA results are given annually ($\Delta t = 1$ a). The MASTER output gives a mean flux values for the whole simulation period. The probability (P_0) of having no impact assuming a Poisson statistic distribution can be calculated, and the probability of having at least one impact is the complement of the collision probability of no impact.

$$\begin{aligned} P_0 &= \exp(-c) \\ P_{\geqslant 1} &= 1 - P_0 = 1 - \exp(-c) \end{aligned} \tag{6}$$

The case in which annual flux and collision rates are given follows the rules for calculating conditional probabilities in which collision probabilities are multiplied. Consequently, the collision probability of no impact after n years (P_{0n}) and the counter example of at least one impact in n years ($P_{\geqslant 1n}$) can be written as

$$\begin{aligned} P_{0n} &= \prod_{i=1}^{n} \exp(-c_i) = \exp\left(-\sum_{i=1}^{n} c_i\right) \\ P_{\geqslant 1n} &= 1 - P_0 = 1 - \exp\left(-\sum_{i=1}^{n} c_i\right). \end{aligned} \tag{7}$$

The results of the collision probability calculation are summarized in Table 2. The table is organized in two row sections, showing the results from LUCA and MASTER for the same cases. The table contains collision probabilities for five test cases. The first two collision probabilities consider the sail and initial condition to exploit the SRP resonance. The first entry, P_{sail}, is the collision probability considering the large sail area. The second entry, P_{mbody}, is the collision probability on the main body but de-orbiting with the sail in resonance. This differentiation is done to separate the sail impacts and main satellite body impacts. Typically, sail impacts are not likely to produce many new fragments, whereas a collision with the main body by a 10 cm impactor will lead to total fragmentation. An impact on the sail might lead to a partial collapse of the sail, reducing the effective area for using the SRP effect.

Table 2
Collision probability comparison.

	Object 1	Object 2	Object 3
	COSMOS 708	STSS Demo 2	R/Sputnik 8
NORAD ID	7663	35937	12998
COSPAR ID	1975-012A	2009-052A	1981-120B
LUCA			
P_{sail}/-	6.7149e−2	7.0351e−1	8.3945e−4
P_{mbody}/–	3.7775e−4	7.5574e−3	1.8442e−5
P_{40}/–	4.3136e−4	1.9383e−3	5.9552e−5
P_{80}/–	9.5670e−4	4.2637e−3	1.2703e−4
P_{120}/–	1.6329e−3	7.2773e−3	1.9274e−4
MASTER			
P_{sail}/–	6.3692e−2	6.8537e−1	1.5424e−3
P_{mbody}/–	3.5766e−4	7.1896e−3	3.3898e−5
P_{40}/–	4.6900e−4	1.9061e−3	5.4869e−5
P_{80}/–	1.0461e−3	4.1748e−3	1.1511e−4
P_{120}/–	1.7554e−3	7.0831e−3	1.7751e−4

The following three rows show the results of the nominal mission (without solar sail) when left in orbit at the catalogued position for 40, 80 and 120 years.

First of all, it can be noted that the values for the probabilities between LUCA and MASTER are very similar. The largest deviations can be seen with the third object which also had the largest spread of the flux values in Fig. 7, bottom graph. Looking at the collision probabilities with the sail, they are, as expected, higher than without sail. For the first object, using a 644 m^2 sail, the collision probability is at 6.5%. The collision probability of the main body remains low, at a comparable level to 40 years in nominal orbit. Regarding the second object, the collision probability for the sail is high: 70% in 68 years until de-orbit, but considering the enhanced A/m ratio of 1 $m^2\,kg^{-1}$ which means a sail of 4580 m^2 The collision probability for the main-body is at the same level as the 120-year probability of the nominal case. The third object has the lowest mass and therefore also the smallest sail of just below 40 m^2. For this object, the values of MASTER are twice as high as the values from LUCA for the sail and main-body analysis. This difference is likely to be caused by statistical nature of the flux values calculated in MASTER. Typically, MASTER flux values are accurate and most meaningful if the target of interest stays in the designated orbit region for longer periods of time (at least several years). Here however, the object is on a SRP augmented re-entry trajectory, a quickly changing descent over time passing through different flux regions. For the nominal case the values from both tools are very similar for the 40-, 80- and 120-year collision probability. The values for the collision probability using the sail (and de-orbiting after 22 years) are roughly one order of magnitude higher than staying in nominal orbit for 60–100 years.

5. Summary and outlook

The results in this paper confirm the possibility of using natural perturbations, in this case SRP and J_2, to reduce remaining orbital lifetime of spacecraft in LEO. This can be achieved by using area augmentation devices, which increase the area-to-mass ratio. Simulations were performed with two orbital propagators to allow cross-validation. The six main resonances could be safely reproduced by both propagators. Near the highly inclined polar orbits, Earth shadowing effects also lead to a favorable increase in eccentricity.

This paper characterizes the one-burn strategies required to target the resonance corridors by performing in plane orbit maneuvers. The orbit evolution inside a resonance is then analyzed and proofs that the 25-year IADC mitigation guideline compliance is possible from orbits above the residual atmosphere.

Currently more sophisticated strategies to exploit the resonances are under development by the astrodynamical partners in ReDSHIFT. The attempt will consider more precise calculation of orbit maneuvers (e.g. out of plane, two-burn strategies, etc.) and the required change in velocity (Schettino et al., 2018). The resulting decision logic will be incorporated in the overall software of ReDSHIFT, which is a main deliverable of the project. The goal of the software is to support mission designers with respect to space debris mitigation and avoidance. It covers not only means of lifetime reduction but will also asses the collision probability and give recommendation for shielding and design-for-demise (Letterio et al., 2018).

The flux assessment of three demonstrative space objects revealed that the flux is higher when an area augmentation device of 1 $m^2\,kg^{-1}$ is used. However, the collision probability of the main body when exploiting the de-orbit highway remains at comparable levels of staying in an unchanged orbit. In prospect of collision modeling in simulations of the space debris environment, this highlights the

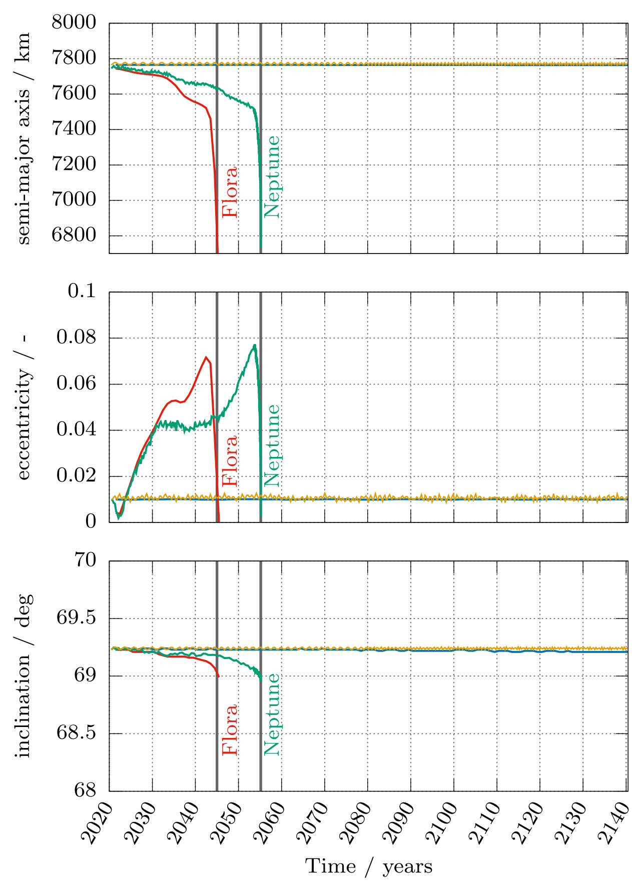

Fig. A.8. Orbit evolution inside the resonance Ψ_4, Object 1 in Table 1: The three plots show the evolution of semi-major axis, inclination and eccentricity over time. In each plot there are four data series present: FLORA results with enhanced A/m ration in red, NEPTUNE with enhanced A/m ration in green, FLORA results with nominal A/m ratio in blue, and NEPTUNE results with nominal A/m ratio in yellow. The plots show that in the enhanced case, both propagators detect the resonance and eventually re-enter after 25 years with FLORA and 35 years with NEPTUNE. In case the nominal A/m ratio is used, the orbit parameters remain essentially constant over time, whereas periodic signatures are clearly visible in the NEPTUNE results. (For interpretation of the references to color in this figure legend, the reader is referred to the web version of this article.)

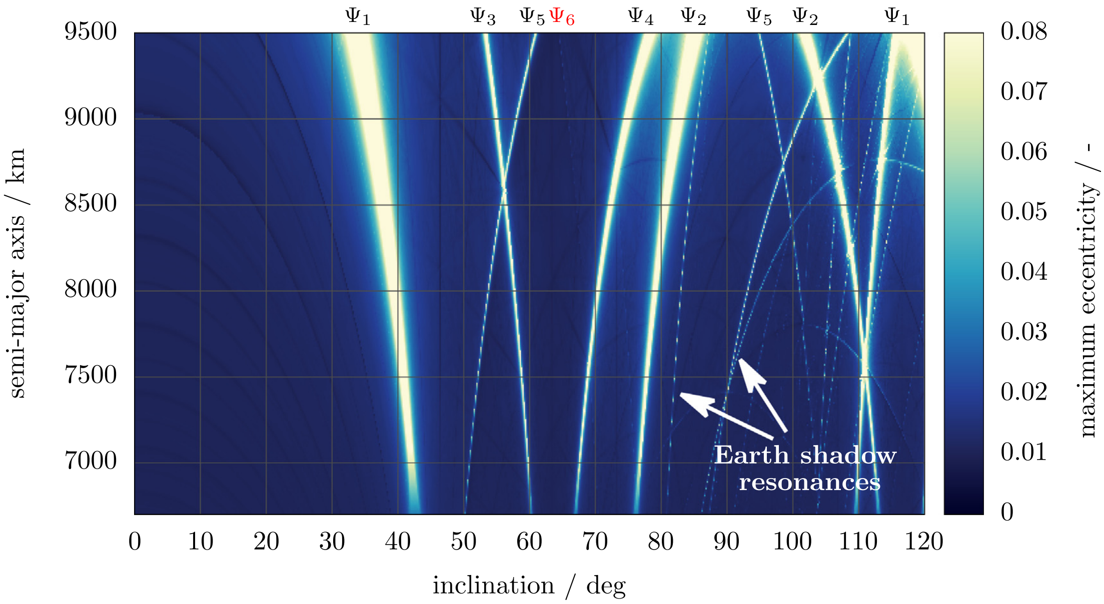

Fig. A.9. SRP resonance with enhanced A/m ratio: The plot shows the maximum eccentricity built-up over 120 years of simulation time with FLORA. The sensitivity for the color range representing the eccentricity built-up now set to 0.01–0.08 which makes also the Ψ_6 resonance appear as faint line.

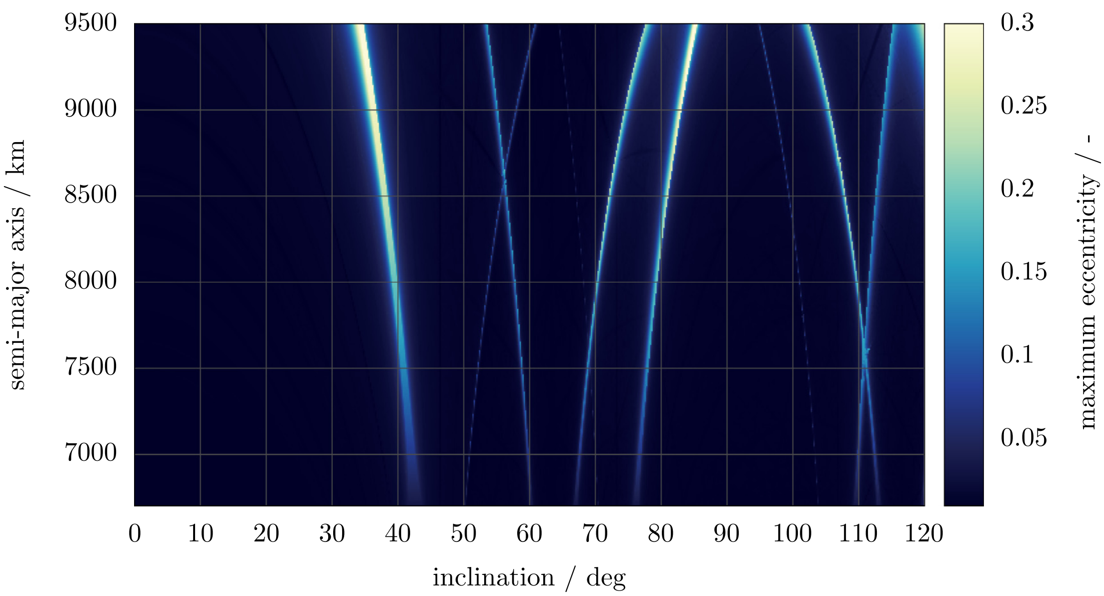

Fig. A.10. FLORA resonance map without the equations for Earth's shadow. The highlighted features between 80° and 100° inclination present in Figs. 2 and A.9 cannot be seen here. This indicates that there are also eccentricity variations due to Earth's shadow which can possibly be used for lifetime reduction.

necessity to discriminate between collisions of the main body (catastrophic, generation of a debris cloud) and the augmented system (non-catastrophic, partial collision with only a few new fragments).

The effects of using the J_2/SRP natural perturbations will be used to derive scenarios for long-term space debris environment studies. This includes cases in which in the future more missions are launched closer to the re-entry corridors, so that more missions can potentially benefit from this effect. We will also perform variations on the amount of Δv available at the end of the nominal operational lifetime of a space mission. It is unlikely that the benefits of using the corridors can be analyzed by simply looking at the overall total number of objects in the space debris environment. Here, more sophisticated ways of presenting the results are necessary and will be developed during the last phase of the project.

Sustainability in outer space activities will become more and more important as the number of space debris is growing, and valuable assets are put at risk. Using natural perturbations as much as possible for shortening the lifetime should be considered if technical feasible and the mission profile allows for it, but it will certainly only be one aspect of debris mitigation strategies.

Acknowledgments

The research leading to these results has received funding from the Horizon 2020 Program of the European Union's Framework Programme for Research and Innovation (H2020-PROTEC-2015) under REA grant agreement n° [687500]- ReDSHIFT.

The authors also express their gratitude to ESA's Space Debris Office for granting permission to use the MASTER 2013 reference population in the context of ReDSHIFT.

Appendix A. Additional plots

See Figs. A.8–A.10.

References

Alessi, E., Rossi, A., Valsecchi, G., Anselmo, L., Pardini, C., Colombo, C., Lewis, H., Daquin, J., Deleflie, F., Vasile, M., Zuiani, F., Merz, K., 2014. Effectiveness of GNSS disposal strategies. Acta Astronaut. 99, 292–302. https://doi.org/10.1016/j.actaastro.2014.03.009.

Alessi, E.M., Schettino, G., Rossi, A., Valsecchi, G.B., 2018a. Natural highways for end-of-life solutions in the LEO region. Celestial Mech. Dyn. Astron. 130, 1–22. https://doi.org/10.1007/s10569-018-9822-z.

Alessi, E.M., Schettino, G., Rossi, A., Valsecchi, G.B., 2018b. Solar radiation pressure resonances in Low Earth Orbits. Mon. Not. R. Astron. Soc. 473, 2407–2414. https://doi.org/10.1093/mnras/stx2507.

Braun, V., 2017. Providing orbit information with predetermined bounded accuracy. Logos Verlag, Berlin. https://doi.org/10.5281/zenodo.228164.

Colombo, C., Alessi, E.M., van der Weg, W., Soldini, S., Letizia, F., Vetrisano, M., Vasile, M., Rossi, A., Landgraf, M., 2015. End-of-life disposal concepts for libration point orbit and highly elliptical orbit missions. Acta Astronaut. 110, 298–312. https://doi.org/10.1016/j.actaastro.2014.11.002.

Colombo, C., Gkolias, I., 2017. Analysis of orbit stability in the geosynchronous region for end-of-life disposal. In: Flohrer, T.E., Schmitz, F.E. (Eds.), Proceedings of the 7th European Conference on Space Debris, ESA Space Debris Office Publishing, Darmstadt, Germany. URL <http://space-debris-conference.com/proceedings/sdc7/paper/864>.

Colombo, C., Rossi, A., Dalla Vedova, F., Braun, V., Bastidavirgili, B., Krag, H., 2017. Drag and solar sail deorbiting: re-entry time versus cumulative collision probability. In: 68th International Astronautical Congress, pp. 25–29.

Cook, G.E., 1962. Luni-solar perturbations of the orbit of an Earth satellite. Geophys. J. Roy. Astron. Soc. 6, 271–291. https://doi.org/10.1111/j.1365-246X.1962.tb00351.x.

Escobal, P.R., 1965. Methods of orbit determination.

Flegel, S., 2007. Simulation of the Future Space Debris Population Considering Mitigation Strategies (in German) – Simulation der zukünftigen Population von Raumfahrtrückständen unter Berücksichtigung von Vermeidungsmaßnahmen Master's thesis. Technische Universität Carolo-Wilhelmina zu Braunschweig.

IADC, 2007. IADC Space Debris Mitigation Guidelines. IADC-02-01, Rev. 1.

Klinkrad, H., 2006. Space Debris: Models and Risk Analysis. Springer, Praxis.

Letterio, F., Alessi, E.M., Gkolias, I., Skoulidou, D., Schaus, V., Beck, J., Vicario de Miguel, G., Schettino, G., Rossi, A., Colombo, C., Tsiganis, K., Holbrough, I., Miguel i Baños, N., 2018. ReDSHIFT software tool for the design and computation of mission end-of-life disposal. In: 7th International Conference on Astrodynamics Tools and Techniques (ICATT), Oberpfaffenhofen, Germany. URL <https://indico.esa.int/event/224/papers/3871/files/209-ICATT-7_2018_ReDSHIFT.pdf>.

Lücking, C., Colombo, C., McInnes, C.R., 2012. A passive satellite deorbiting strategy for medium Earth orbit using solar radiation pressure and the J2 effect. Acta Astronaut. https://doi.org/10.1016/j.actaastro.2012.03.026.

Möckel, M., 2015. High Performance Propagation of Large Object Population in Earth Orbits (Ph.D. thesis). Fakultät für Maschinenbau, Technische Universität Braunschweig.

Moxnes, J.F., Frøyland, Ø., Øye, I.J., Brate, T.I., Friis, E., Ødegårdstuen, G., Risdal, T.H., 2017. Projected area and drag coefficient of high velocity irregular fragments that rotate or tumble. Defence Technol. 13, 269–280. https://doi.org/10.1016/j.dt.2017.03.008.

Musen, P., 1960. The influence of the solar radiation pressure on the motion of an artificial satellite. J. Geophys. Res. 65, 1391–1396. https://doi.org/10.1029/JZ065i005p01391.

Oltrogge, D.L., Chao, C.C., 2007. Standardized approaches for estimating orbit lifetime after end-of-life. In: AAS/AIAA Astrodynamics Specialist Conference, Mackinac Island, MI. Published in 2008 in Advances in the Astronautical Sciences Series 129 Part 1, pp. 187–206.

Parkinson, R.W., Jones, H.M., Shapiro, I.I., 1960. Effects of solar radiation pressure on Earth satellite orbits. Science 131, 920 LP–921 LP. https://doi.org/10.1126/science.131.3404.920.

Öpik, E.J., 1951. Collision probabilities with the planets and the distribution of interplanetary matter. Proc. Roy. Irish Acad. Sect. A: Math. Phys. Sci. 54, 165–199.

Rossi, A., Colombo, C., Tsiganis, K., Beck, J., Rodriguez, J.B., Walker, S., Letterio, F., Dalla Vedova, F., Schaus, V., Popova, R., Francesconi, A., Stokes, H., Schleutker, T., Alessi, E.M., Schettino, G., Gkolias, I., Skoulidou, D.K., Holbrough, I., Bernelli Zazzera, F., Stoll, E., Kim, Y., 2018. Redshift: a global approach to space debris mitigation. Aerospace 5. https://doi.org/10.3390/aerospace5020064 <http://www.mdpi.com/2226-4310/5/2/64> .

Schaus, V., Radtke, J., Stoll, E., Rossi, A., Colombo, C., Tonetti, S., Holbrough, I., 2017. Results of reference long-term simulations focussing on passive means to reduce the impact of space debris. In: Flohrer, T.E., Schmitz, F.E. (Eds.), Proceedings of the 7th European Conference on Space Debris, ESA Space Debris Office Publishing, Darmstadt, Germany. URL <http://space-debris-conference.com/proceedings/sdc7/paper/342>.

Schettino, G., Alessi, E.M., Rossi, A., Valsecchi, G.B., 2018. Exploiting dynamical perturbations for the end-of-life disposal of spacecraft in LEO. Astronomy and Computing Manuscript submitted and under final review.

Skoulidou, D., Rosengren, A.J., Tsiganis, K., Voyatzis, G., 2017. Cartographic study of the MEO phase space for passive debris removal. In: Flohrer, T.E., Schmitz, F.E. (Eds.), Proceedings of the 7th European Conference on Space Debris, ESA Space Debris Office Publishing, Darmstadt, Germany. URL <http://space-debris-conference.com/proceedings/sdc7/paper/670>.

Vallado, D.A., 2013. Fundamentals of Astrodynamics and Applications, fourth ed. Microcosm Press.